

## Article

# Fluctuation Analysis of Centrosomes Reveals a Cortical Function of Kinesin-1

Franziska Winkler,<sup>1</sup> Maheshwar Gummalla,<sup>1</sup> Lutz Künneke,<sup>2</sup> Zhiyi Lv,<sup>1</sup> Annette Zippelius,<sup>2</sup> Timo Aspelmeier,<sup>3,4</sup> and Jörg Grosshans<sup>1,\*</sup>

<sup>1</sup>Institute for Developmental Biochemistry, Medical School, <sup>2</sup>Institute for Theoretical Physics, <sup>3</sup>Institute for Mathematical Stochastics, and <sup>4</sup>Felix Bernstein Institute for Statistics in the Biosciences, Georg-August-University Göttingen, Göttingen, Germany

**ABSTRACT** The actin and microtubule networks form the dynamic cytoskeleton. Network dynamics is driven by molecular motors applying force onto the networks and the interactions between the networks. Here we assay the dynamics of centrosomes in the scale of seconds as a proxy for the movement of microtubule asters. With this assay we want to detect the role of specific motors and of network interaction. During interphase of syncytial embryos of *Drosophila*, cortical actin and the microtubule network depend on each other. Centrosomes induce cortical actin to form caps, whereas F-actin anchors microtubules to the cortex. In addition, lateral interactions between microtubule asters are assumed to be important for regular spatial organization of the syncytial embryo. The functional interaction between the microtubule asters and cortical actin has been largely analyzed in a static manner, so far. We recorded the movement of centrosomes at 1 Hz and analyzed their fluctuations for two processes—pair separation and individual movement. We found that F-actin is required for directional movements during initial centrosome pair separation, because separation proceeds in a diffusive manner in latrunculin-injected embryos. For assaying individual movement, we established a fluctuation parameter as the deviation from temporally and spatially slowly varying drift movements. By analysis of mutant and drug-injected embryos, we found that the fluctuations were suppressed by both cortical actin and microtubules. Surprisingly, the microtubule motor Kinesin-1 also suppressed fluctuations to a similar degree as F-actin. Kinesin-1 may mediate linkage of the microtubule (+)-ends to the actin cortex. Consistent with this model is our finding that Kinesin-1-GFP accumulates at the cortical actin caps.

## INTRODUCTION

The syncytial embryo of *Drosophila* is a system well suited to the investigation of cytoskeletal networks and functional interactions between microtubule asters and actin cortex. As no cell membranes separate the cellular units, the cytoskeleton forms a potentially large network extending over the whole embryo (1,2). Microtubule asters with a pair of centrosomes in their center overlap with neighboring asters, thus forming a network. Each microtubule aster is associated with a nucleus. Network behavior is reflected by nuclear dynamics in syncytial embryos. The nuclei form an array that undergoes cell-cycle-dependent movements and cycles between unordered and ordered arrangements (3). Nuclear dynamics is associated with fast stereotypic changes of the cytoskeleton. Within minutes, microtubules switch between spindles in mitosis and asters in interphase, whereas F-actin switches from cortical caps in interphase to furrows in mitosis. Microtubules and cortical actin interact functionally. Besides being

organizers of the microtubule asters, centrosomes induce the formation of cortical actin caps (4), whereas F-actin is required for cortical anchoring of the microtubule network. During interphase, the cortical link is important for positioning and separation of centrosome pairs. After duplication in early interphase, the two daughter centrosomes move apart. Before nuclear envelope breakdown, they move to the equator of the associated nucleus (1). The equatorial movement depends on actin polymerization by Dia and Arp2/3 as well as the molecular motors Myosin-II and Dynein (5–7). It is unknown, however, whether and how the actin cortex contributes to initial separation of centrosome pairs and to dynamics of centrosomes and microtubule asters in interphase.

Active cytoskeletal networks in cells are far away from the thermodynamic equilibrium. Despite this, the cytoskeleton acquires stable steady-state structures on a timescale longer than minutes. In contrast, at short timescales in the millisecond range, thermal diffusion may dominate. In the intermediate range of seconds, fluctuations of the network may reflect the active nonequilibrium dynamics of the cytoskeleton (8). Molecular motors are a potential driving force for the dynamics of cytoskeletal networks. Although filament dynamics has been well characterized, the behavior of networks within a cell on a timescale of seconds, to our

Submitted October 14, 2014, and accepted for publication July 31, 2015.

\*Correspondence: [jgrossh@gwdg.de](mailto:jgrossh@gwdg.de)

This is an open access article under the CC BY-NC-ND license (<http://creativecommons.org/licenses/by-nc-nd/4.0/>).

Franziska Winkler, Maheshwar Gummalla, and Lutz Künneke contributed equally to this work.

Editor: Margaret Gardel.

© 2015 The Authors  
0006-3495/15/09/0856/13

<http://dx.doi.org/10.1016/j.bpj.2015.07.044>



knowledge, has been little investigated. Thus, analysis of trajectories and fluctuations of centrosomes may provide information about microtubules network organization and interactions between individual asters and with the actin cortex, which goes beyond information obtained from static images.

Kinesin-1 is the prototype of the (+)-end directed microtubule motors (9). In *Drosophila*, Kinesin-1 is required for transport of determinants for patterning of the embryonic axes (10,11), axonal transport, and distribution of nuclei in syncytial muscle (12,13). Kinesin-1 acts together with Enscosin (ens), which loads Kinesin-1 onto microtubules (12,14). A function of Kinesin-1 in syncytial embryos has not been investigated, yet.

Here, we establish fluctuation analysis of centrosome dynamics to reveal mechanisms driving the initial separation of centrosome pairs and centrosome movement in interphase. With these analyses and by applying a mechanical model, we found that F-actin provides directed forces for initial pair separation in contrast to separation by random interactions. By fluctuation analysis of centrosomes in interphase, we revealed that cortical actin caps and, surprisingly, the microtubule motor Kinesin-1 as well, suppress centrosome fluctuations. Based on this and additional genetic data, we propose a model in that Kinesin-1 mediates linkage of the microtubule network to the actin cortex to stabilize the microtubule network and the associated nuclear array.

## MATERIALS AND METHODS

### *Drosophila* genetics

The following mutations and fly strains were used: FRT[G13], *Khc*<sup>27</sup> (14), *ens*<sup>swa</sup> (12), Dmn-GFP (Dynamitin) (15), Dlc-GFP (Dynein light chain), Kinesin-1-GFP (14), Sas6-GFP (16), Sas4-GFP (16), and *ced-12/ELMO*<sup>367</sup> (EMS mutant isolated in a screen for blastoderm mutations in germline clones (17). MTD-Gal4 (maternal GAL4) (18), *Kinesin-1* RNA<sub>i</sub> (PTRiP: GL00330attP2; Transgenic RNA<sub>i</sub> Resource Project, Harvard Medical School, Boston, MA), Utrophin-GFP (19), and Zipper-GFP (*zip*<sup>CC01626</sup>, Bloomington *Drosophila* Stock Center, Indiana University, Bloomington, IN). *Kinesin-1* depleted embryos were obtained from females carrying one copy of each of the following: the *Kinesin-1* RNA<sub>i</sub>, the MTD-Gal4, and either Sas4-GFP, Dlc-GFP, or Dmn-GFP transgenes. *Kinesin-1* depleted embryos were recognized by their cellularization defect. Germline clones were generated by FRT/Flipase-mediated mitotic recombination and selection with *ovo*<sup>D</sup>. The *ELMO*<sup>367</sup> lethality and blastoderm phenotypes were mapped by meiotic recombination to the *b* region. The lethality was fine-mapped to a 43kb region by noncomplementation with molecularly defined deficiencies available from the Bloomington *Drosophila* Stock Center. *ELMO*<sup>367</sup> is an allele of *ELMO* as it did not complement the c06760 allele, whereas mutations of the other genes in the region were complemented.

### Molecular genetics

The *Ubiquitin* promoter (*PstI-BgIII*) (20), *Drosophila* dynein light chain (*SacII-BamHI*) (21), and eGFP (*BamHI-BamHI-KpnI*) were inserted between the *PstI-KpnI* sites of a pUAS derivative lacking the UAS and hsp70TATA sites. PCR cloning was verified by sequencing of all fragments.

## Histology

Embryos were fixed by 4% formaldehyde (37% for microtubules staining) and stained according to standard procedures (22). F-actin was detected with labeled phalloidin (Invitrogen, Carlsbad, CA) and DAPI (0.2 μg/mL). The following antibodies were employed: monoclonal anti-α-Tubulin (Sigma-Aldrich, St. Louis, MO) and goat IgGs coupled with Alexa dyes (at final 4 μg/mL, Invitrogen).

## Microinjection

Dechorionated embryos were aligned on a coverslip, briefly desiccated, and covered with halocarbon oil (Votalef 10S; Lehmann & Voss, Hamburg, Germany). Colcemid (100 mg/mL; CalbioChem, San Diego, CA), Latrunculin A (100 mg/mL; Cayman Chemical, Ann Arbor, MI), Jasplakinolide (1 mM), or Y-27632 (10 mM, Sigma-Aldrich) were injected into Sas6-GFP-expressing embryos. Time-lapse recording was started immediately after injection. *Slam* dsRNA was synthesized and injected as described previously in Wenzl et al. (22). Latrunculin A, colcemid, and Y-27632 activities were verified by injection into embryos expressing Utrophin-GFP, Tubulin-GFP, and Zipper-GFP, respectively. Jasplakinolide activity was verified by fluorescence-recovery-after-photobleach analysis in Utrophin-GFP-expressing embryos. Injection of latrunculin A before onset of anaphase induced a nuclear fallout phenotype with approximately one-half of the nuclei and their centrosomes falling into the interior of the embryo. After colcemid injection, the centrosomes were not able to separate from each other in the following mitosis. Sodium azide (0.02% in water) was injected in Sas4-GFP-expressing embryos in mitosis interphase 13. Recording was started 3 min after injection.

## Microscopy

Time-lapse recording was performed with an inverted microscope with a spinning disk unit (model No. CSU-X1; Carl Zeiss, Jena, Germany) and an AxioCam MRm camera (Carl Zeiss). The temperature was 20–23°C. Seven to nine sections covering ~2 μm were recorded with a EC Plan Neo-Fluar objective (40×/NA1.3/oil; Carl Zeiss) at a frame rate of 1 Hz for up to 20 min with an exposure time of 30 ms. The stack size of 2 μm corresponds to ~2.5% of the embryonic radius. Thus, perspective distortions at the edges were <2.5%, allowing us to treat the images as two-dimensional. For fast imaging at 20 Hz, single planes were recorded for 5 min with a PlanApochromat lens (100×/NA1.4/oil; Carl Zeiss) and an electron-multiplying charge-coupled device camera (Evolve 512; Photometrics, Huntington Beach, CA). A 20-Hz recording was started shortly after start of centrosome duplication, when centrosomes stopped moving in the apical-basal direction. The *CZI* files with the original data were exported into *omeTIF* files, and imported into the software IMAGEJ (National Institutes of Health, Bethesda, MD) as 16-bit TIFF stacks. The Z sections were fused using the GROUPED Z project option of IMAGEJ. Fixed embryos and movies of Kinesin-1-GFP, Dlc-GFP, and Dmn-GFP were recorded with a confocal microscope (model No. LSM780, Plan ApoChromat lens, 63×, NA1.4, oil; Carl Zeiss). For low illumination conditions, the laser intensity was reduced to one-third of the normal intensity.

## Image analysis and tracking

Each image, in a time series of fluorescence microscopic images taken of an embryo, consists of a (typically nonzero) background signal and a number of bright spots, each of which is created by a fluorescence-labeled centrosome. Due to the diffraction limit of the optical microscope, these spots are not pointlike but blurred by a point-spread function *h* over a region of a diameter of ~300 nm in the image, corresponding to several pixels. Furthermore, the image is noisy due to the fact that the fluorophores emit photons in a statistical manner. This leads to Poisson noise in the image,

and one of the consequences of this is the fact that the relative strength of the noise increases with decreasing light intensity, which limits the frame rate (i.e., the exposure time per frame) of the movies. We hence have the image generation model

$$I_t(x) \sim \text{Poisson}((h \times f_t)(x) + b_t(x)),$$

where  $x$  is the location of an image pixel,  $I_t(x)$  is the measured signal at time  $t$ , pixel  $x$ ,  $f_t$  is the density of centrosomes at time  $t$ , and  $b_t$  is the background signal at  $t$ . The asterisk symbol (\*) is the convolution operator.

To be able to identify the individual centrosomes reliably even when the intensity is low or when a centrosome is poorly lit due to a statistical fluctuation, it is necessary to employ a method that takes the image generation process and noise characteristics into account. Therefore, we adapted a maximum likelihood approach. In this approach, one tries to find the  $\hat{f}_t, \hat{b}_t$  configuration of centrosomes that maximizes the conditional probability  $P(I_t | \hat{f}_t, \hat{b}_t)$  of obtaining the actually observed image, i.e.,

$$(\hat{f}_t, \hat{b}_t) = \arg \min_{(f', b')} (-\log(P(I_t | f', b'))).$$

This method alone, however, is not sufficient, as there are two additional difficulties. First, the blurring of the image by the microscope destroys information on small length scales (smaller than the size of the spots). This is especially important when the centrosomes are close to each other, which is the case just after centrosome doubling. In particular, without further help, the method cannot decide whether there are one, two, or more centrosomes hidden under a spot. Second, there is the background signal, which complicates centrosome detection because a naive implementation of the above scheme would attribute a local signal to either the background signal or the centrosome density (or both); however, we would have no way of knowing which is correct. Incidentally, the background signal also makes centrosome identification by other methods (such as thresholding) difficult because it varies from movie to movie, from frame to frame, and also within each frame. For centrosome detection, the background must therefore be included in the image analysis.

The difficulties can be surmounted by supplying additional information to the method in the form of sparsity constraints. From the knowledge of the system being observed it is clear that the density of centrosomes is sparse, i.e., the number of centrosomes in each image is much less than the number of pixels in each image. It is also clear that the background signal is very smooth, i.e., slowly varying in space (in contrast to the signal caused by the centrosomes, which is strongly peaked). This smoothness of the background signal can be modeled by sparsity of the spatial Fourier transform of  $b$  (23). Hence our method of centrosome detection consists of the maximum likelihood method, augmented by sparsity enforcing terms, so our estimate of the centrosome density (and the background signal) is

$$(\hat{f}_t, \hat{b}_t) = \arg \min_{f', b'} (-\log(P(I_t | f', b')) + \lambda_1 \|f'\|_1 + \lambda_2 \|\tilde{b}'\|_1), \quad (1)$$

with the additional constraint that  $f'(x), b'(x) \geq 0$  for all  $x$ . Here, the 1-norm is defined by  $\|f'\|_1 = \sum_x |f'(x)|$  and analogously for  $\tilde{b}'$ , the Fourier transform of  $b'$ . The constants  $\lambda_1, \lambda_2 > 0$  are suitably chosen parameters, which depend, among other things, on the background intensity, its variation, or the signal strength. In this work, we determined the values empirically. Automatic data-driven parameter selection would also be feasible, e.g., by cross-validation (24) or by statistical multiscale methods (25), but this was not the focus of this article. Approaches related to the one presented here have been suggested in the context of superresolution microscopy (26–28).

The terms involving the 1-norms have the effect of forcing most entries of  $f'$  and  $\tilde{b}'$  to 0. They are convex functionals, such that this procedure amounts to a convex optimization problem, for which efficient numerical

methods exist. We chose the alternating direction of multipliers method (29), which works well for this case.

When the density  $\hat{f}_t$  is found by minimizing Eq. 1, we extract a list of centrosome positions from the nonzero entries of  $\hat{f}_t$ . The centrosomes in successive frames are then matched to each other by a proximity criterion, thus forming individual time tracks. When centrosome doubling occurs, this is recognized by the fact that a new track starts in midmovie, and its partner is determined as the closest centrosome at the time of the appearance of the track. Because centrosome identification can sometimes fail despite all efforts, we also employ corrections for the cases when centrosomes are missing in individual frames.

In some of our figures, the data are plotted as a function of the time after splitting. This refers to the time elapsed since a centrosome was last seen to duplicate. Each centrosome is hence assigned its individual time by setting its internal clock to 0 at the time of the last split. In this way, we can aggregate information from different times and different positions on the embryo, but which has a functional correspondence.

## Fluctuations

In Fig. 1 A, a typical time track of a centrosome pair is shown. Clearly, the motion of the centrosomes undergoes some sort of smooth directed motion with nonsmooth fluctuations about it. Our interest here is not the drift motion but rather the fluctuations.

Often, the mean-square displacement is used for analysis in particle tracking (30). As the smooth part of the motion is, in our case, very irregular (it varies strongly between centrosomes and it sometimes reverses direction, for example), we found it convenient to quantify the fluctuations directly by differencing, namely by considering the quantity (see Fig. 2 A) (31),

$$D_i(t_j) = \frac{(\vec{d}_i(t_j))^2}{\Delta t} \quad \text{with} \quad (2)$$

$$\vec{d}_i(t_j) = \vec{r}_i(t_j) - \frac{1}{2}(\vec{r}_i(t_{j-1}) + \vec{r}_i(t_{j+1})),$$

where  $\vec{r}_i(t)$  is the trajectory of centrosome  $i$  and  $t_1, t_2, \dots$  are the times at which the frames were taken. We assume that the frames were recorded equidistantly such that  $t_{i+1} - t_i = \Delta t$  with the same  $\Delta t$  for all frames.

This quantity has the advantage that any smooth drift movement is removed to a very good approximation by taking the difference between the position of a centrosome at an intermediate time  $t_j$ , and the average position of the adjacent times  $t_{j-1}$  and  $t_{j+1}$ , if the time increment  $\Delta t$  is small enough such that the drift does not change appreciably in that interval.

To illustrate this behavior, we consider the simple case that  $\vec{r}_i(t)$  undergoes Brownian motion in a flow field  $\vec{v}(\vec{r}, t)$ . Dropping the particle index  $i$ , this can be described by the Langevin equation

$$\frac{d\vec{r}}{dt} = \vec{v}(\vec{r}, t) + \gamma \vec{\xi}(t), \quad (3)$$

where  $\vec{\xi}$  is Gaussian random noise with average  $\mathbb{E}(\vec{\xi}(t)) = 0$  and  $\mathbb{E}(\xi_\alpha(t) \xi_\beta(t')) = \delta_{\alpha\beta} \delta(t - t')$  (here and in the following, the symbol  $\mathbb{E}$  denotes the average), and  $\gamma > 0$  is the noise strength. For a spatially and temporally constant flow field  $\vec{v}(\vec{r}, t) = \vec{v}_0 = \text{const.}$ , the motion over a time interval  $\Delta t$  is given by  $\vec{r}(t_{j+1}) = \vec{r}(t_j) + \vec{v}_0 \Delta t + \vec{b}(t_j)$ , where the increment  $\vec{b}$  is a Gaussian random vector with covariance  $\gamma^2 \Delta t I_2$ , with  $I_2$  being the  $2 \times 2$  identity matrix. Increments at different times  $t_j, t_{j+1}, t_{j+2}, \dots$  are independent from each other. Inserting this into the expression for  $\vec{d}_i(t_j)$  shows that the flow vector  $\vec{v}_0$  drops out completely and only the increments remain. Taking the average over the Gaussian distributions of the increments then yields the diffusion constant

$$\mathbb{E} D_i(t_j) = \gamma^2,$$

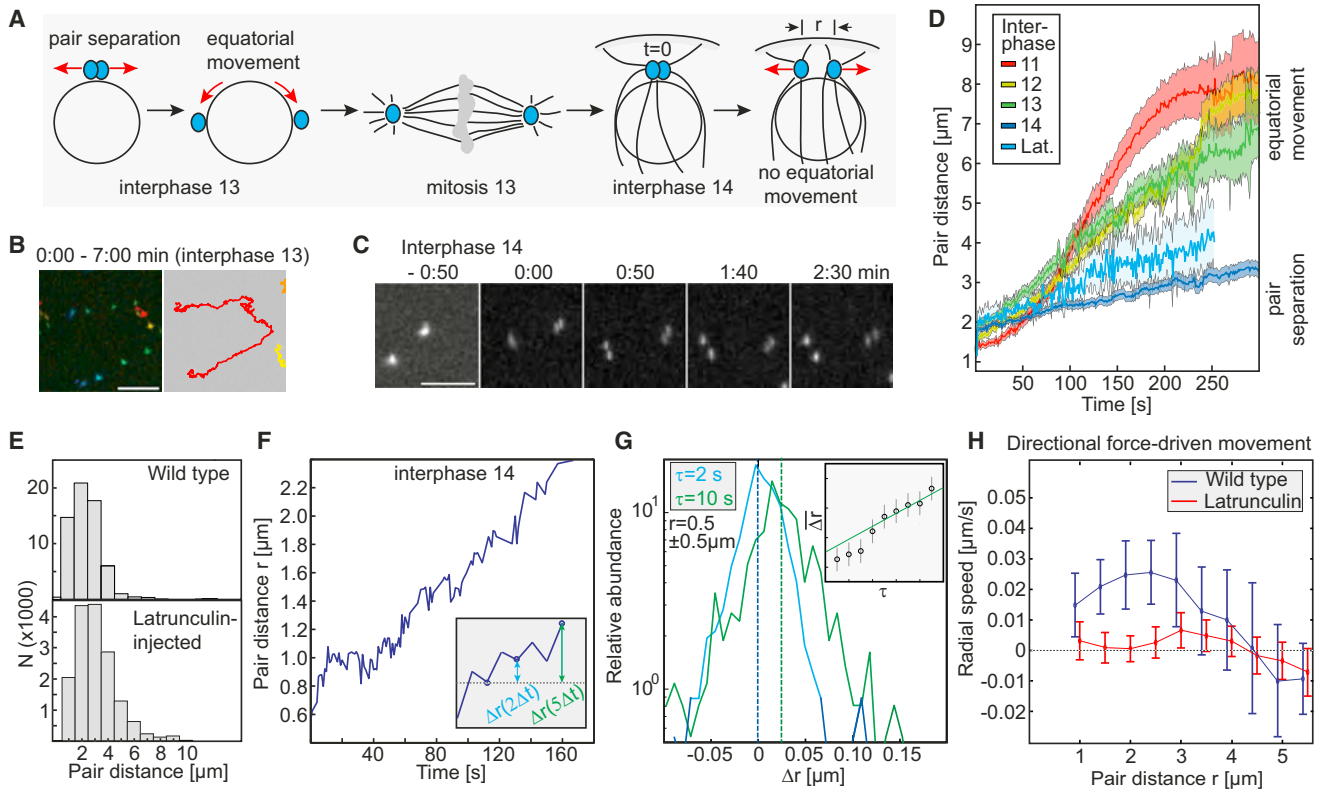


**FIGURE 1** Directional F-actin-dependent movement during initial centrosome separation. (A) Schematic drawing of centrosome (blue) cycle. Spindle pole position in mitosis, showing position between plasma membrane and nucleus during interphase. Duplication of centrosome in early interphase and pair separation before mitosis. (Red arrows) Centrosome movement. (B) Trajectory of a centrosome pair (red). (Color-coding from red to blue) Direction of path between 0:00 and 7:00 min. Scale bar = 5  $\mu\text{m}$ . (C) Images from movie of centrosomes marked with SAS-6-GFP. Scale bar = 5  $\mu\text{m}$ . (D) Pair distance (average, standard deviation) of centrosome pairs during interphases 1–14 and latrunculin-injected embryos in cycle 14. (E) Histograms of pair distances for interphase 14 in wild-type and latrunculin-injected embryos. (F) Representative trace of a single centrosome pair. (Inset) Illustration of the definition of the pair-distance changes  $\Delta r$  as a function of elapsed time  $\tau$ . (G) Distributions of pair-distance changes  $\Delta r$  for the indicated range of initial pair distances and elapsed times  $\tau$ . (Dashed lines) Respective averages of  $\overline{\Delta r}$ . (Inset)  $\overline{\Delta r}$  varies linearly with  $\tau$ . Exemplary data set. (H) Average radial speed dependent upon pair distance for centrosomes in wild-type (blue) and latrunculin-injected (red) embryos.

independent of  $\Delta t$ . Of course, in our experiments we cannot assume that the motion is truly Brownian (see, e.g., Lau et al. (32) and Wessel et al. (33)), hence we prefer the term “fluctuations” for the quantity  $D_i(t_j)$  rather than “diffusion constant”. However, the ability of the fluctuation parameter  $D$  to separate fast random fluctuations from slowly changing drift movement is not limited to this simplified Langevin model but remains valid in more complicated cases, provided there is a sufficient separation of timescales between the two.

In practice, there is always a measurement error associated with the position measurements  $\vec{r}_i(t)$  such that  $\vec{r}'_i(t) = \vec{r}_i(t) + \sigma \vec{\epsilon}_i(t)$  is observed, where  $\sigma$  is the magnitude of the error and the  $\vec{\epsilon}_i(t)$  can be approximated by independent Gaussian random vectors with covariance  $I^2$  (but see Savin and Doyle (34,35) for a detailed discussion of possible measurement errors and their implications). Inserting  $\vec{r}'_i$  in place of  $\vec{r}_i$  in Eq. 2 yields the observed

$$\vec{d}'_i(t_j) = d_i(t) + \sigma \vec{\epsilon}_i(t_j) - \frac{\sigma}{2} (\vec{\epsilon}_i(t_{j-1}) + \vec{\epsilon}_i(t_{j+1})).$$

The  $E$  values can be combined into one effective random vector  $\vec{\eta}_i(t_j) = \vec{\epsilon}_i(t_j) - (1/2)(\vec{\epsilon}_i(t_{j-1}) + \vec{\epsilon}_i(t_{j+1}))$ , which is a Gaussian random vector with covariance  $(3/2)I_2$ . The observed fluctuations  $D'_i(t_j)$  hence acquire an additional noise contribution,  $D'_i(t_j) = ((\vec{d}_i(t_j) + \sigma \vec{\eta}_i(t_j))^2) / \Delta t$ . Denoting the average over the measurement error by an overbar, we obtain

$$\overline{D'_i(t_j)} = D_i(t_j) + 3 \frac{\sigma^2}{\Delta t}. \quad (4)$$

Hence a nonzero measurement error  $\sigma$  makes the observed fluctuation  $D'_i(t_j)$  diverge as  $\Delta t$  goes to zero. In practice, therefore, we need to seek an appropriate  $\Delta t$ , which is small enough for  $D_i(t_j)$  to be insensitive to the drift and large enough to be insensitive to measurement error. This issue is addressed in the Results.

For testing whether the mean value of the fluctuations for two different treatments can be considered to be equal, we used Welch’s  $t$ -test. Under the null hypothesis that the means are equal, the observed data would have had a probability  $p$  of occurring, where  $p$  is the respective  $p$ -value listed in Table S3. The MATLAB function  $t$ -test2 was used for the actual calculations.

## Simulation of fluctuations

To distinguish the qualitative behavior of the fluctuations for different types of movements, we performed simulations on a simplified model system of  $n$  pointlike objects in the plane. There are no interactions between particles but each particle performs a random (Brownian) movement plus a drift. Because the particles do not interact, we focus on one particular particle. That particle’s position  $\vec{r}(t)$  is then described by Eq. 3. In addition to the

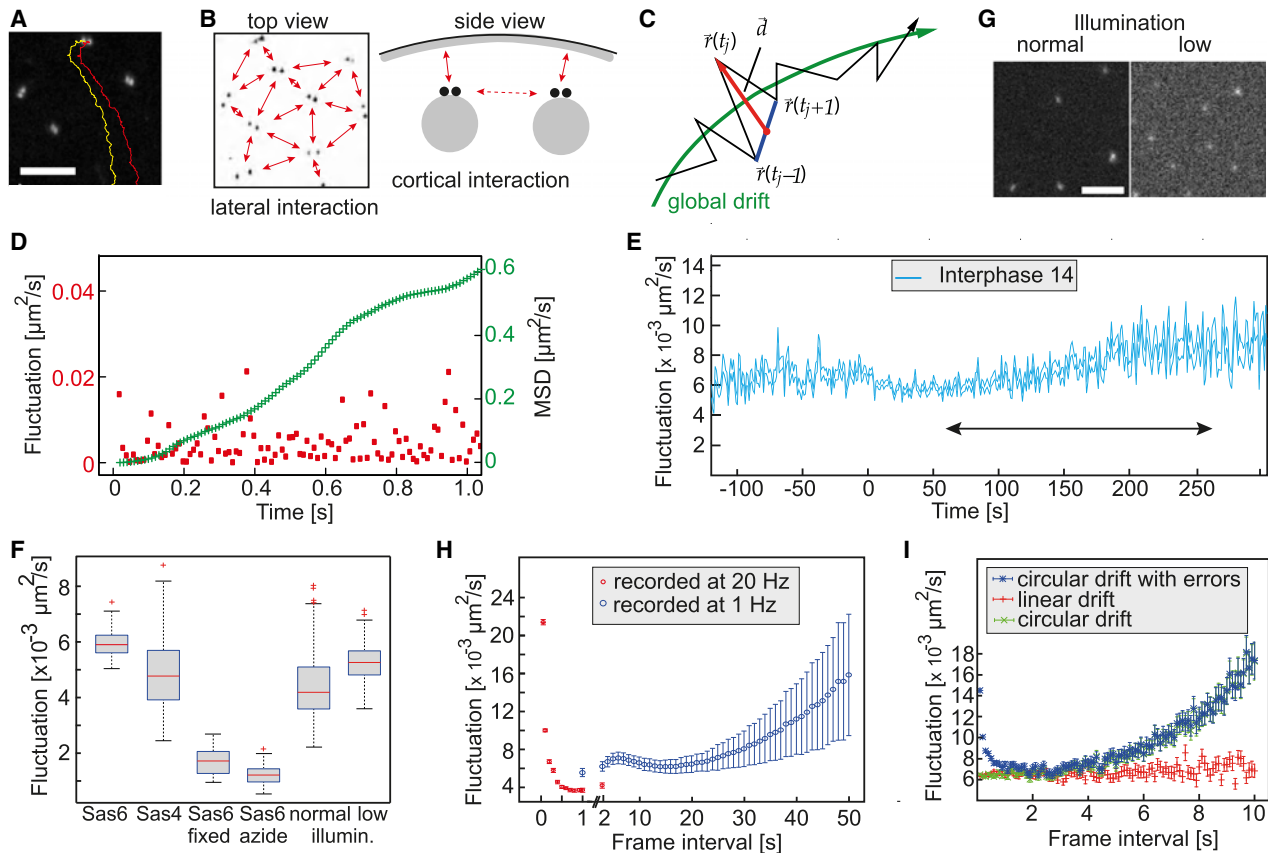


**FIGURE 2** Fluctuation parameters. (A) Traces (yellow and red) of a centrosome pair over two minutes. (B) Lateral and cortical interactions (arrows in red) determine mobility of centrosome pairs (black disks) and their associated nuclei (gray disk). (C) Definition of the fluctuation parameter  $D$ . (D) Comparison of MSD (green) and fluctuation parameter (red). As the simulations are based on manually chosen parameters, the resulting absolute numbers may differ from the experiments. (E) Averaged time course of  $D$  (range of standard deviation). The value  $t = 0$  represents time of centrosome splitting. (Arrow in black) Averaged period (60–260 s). (F) Time-averaged fluctuation (60 s  $< t < 260$  s). Sas4-GFP and Sas6-GFP are two centrosome markers. (F and G) Images with normal and low (one-third of laser intensity) illumination. (H) Dependence of  $D$  (average and standard deviation) on the frame interval for data sets recorded at a frame rate of 20 Hz (red) and 1 Hz (blue). (I) Dependence of  $D$  on the frame interval calculated with computed data sets containing fluctuations with linear drift (red), fluctuations with circular drift (green), and fluctuations with circular drift and measurement error (blue). Scale bars = 5  $\mu\text{m}$ .

stochastic forces  $\vec{\xi}$ , we also allow for measurement errors as in Fluctuations, described above, by recording  $\vec{r}'(t) = \vec{r}(t) + \sigma\vec{\epsilon}(t)$ , i.e., a noisy version of the true position  $\vec{r}(t)$ .

For the flow field  $\vec{v}(\vec{r}, t)$ , we chose two variants. The first is a constant linear drift,  $\vec{v}(\vec{r}, t) = \vec{v}_0$ . According to our construction of the fluctuation parameter  $D$ , such a linear drift will have no influence on the measurements of  $D$ , irrespective of  $\Delta t$ . The second variant is a circular flow field,  $\vec{v}(\vec{r}, t) = c\vec{r}^\perp(\vec{r})$ , where  $c > 0$  is a constant and  $\vec{r}^\perp(\vec{r})$  is defined for  $\vec{r} = (x, y)^T$  by  $\vec{r}^\perp(\vec{r}) = (-y, x)^T$ . For the simulations shown below, we used the values  $\gamma = 0.08 \mu\text{m}/\sqrt{\text{s}}$ ,  $\vec{v}_0 = (-0.04, 0.04)^T \mu\text{m}/\text{s}$ , and  $c = 0.04 / \text{s}$ . The values for  $\vec{v}_0$  and  $c$  were chosen such that the magnitude of the velocity field roughly agrees with estimates of typical drift velocities in experiments.

From a simulation of these equations, we obtained a time series of simulated measured particle positions  $\vec{r}(t)$  (corresponding to  $\sigma = 0$ ) and its noisy version  $\vec{r}'(t)$  (corresponding to  $\sigma > 0$ ), and then calculated the noiseless fluctuation parameter  $D(t)$  and its noisy counterpart  $D'(t)$  for the simulated particle for different values of  $\Delta t$ . For each  $\Delta t$ , these values were averaged over  $t$  to obtain a  $D$  as a function of  $\Delta t$ , as shown in Fig. 2 I.

In the linear drift case, and with  $\sigma = 0$ , there are no measurement errors, only fluctuations (this type of behavior is marked as *linear drift* in Fig. 2 I). As expected, the fluctuation parameter in this case does not depend on  $\Delta t$  because the assumption of a spatially and temporally constant drift

is satisfied. The measured value agrees with the expected value of  $\gamma^2 = 0.0064 \mu\text{m}^2/\text{s}$ .

In the case of the circular drift, and with  $\sigma = 0$ , the fluctuations  $D$  coincide with the case of the linear drift for small  $\Delta t < 3$  s, as expected (*circular drift* in Fig. 2 I). In the opposite case, the time interval  $\Delta t$  is so large that the assumption of homogeneous drift breaks down and the measured values of  $D$  deviate from the ideal value.

When measurement errors are switched on for the circular drift (we chose  $\sigma = 0.016 \mu\text{m}$ , which is approximately the size of a pixel in the experiments), the values of  $D$  also start to deviate noticeably from the ideal value for small  $\Delta t < 1$  s (*circular drift with errors* in Fig. 2 I). However, in the intermediate regime between 1 and 3 s, the estimation of  $D$  works reliably.

### Radial speed: a qualitative measure for centrosomal forces

When we consider the process of separation of the centrosome pairs, we observe the following behavior. Each pair of centrosomes has a time-dependent distance (Fig. 1 C). We locate all events in space and time where a pair has an intrapair distance within a small interval around some  $r_0$  and then make a histogram of their distance a certain time  $\tau$  later. Such a histogram is shown in Fig. 1 G. We observe that the width of this histogram increases

with  $\tau$ , which is a sign of a diffusionlike process. In addition, the location of the average of the histogram moves toward greater distances. This is the signature of a force-driven process: without a force acting, there would be no change in the average pair distance. However, this is only strictly true for short times  $\tau$  because for longer times the distribution of the distance would reach the minimal value of 0 where additional effects become relevant. Hence, we can interpret the radial speed  $v_{r_0}$  defined by the speed of the average of the intrapair distance after an initial separation of  $r_0$  as a measure of the force acting at a distance of  $r_0$ . In a purely viscous system with Gaussian random forces, this analogy would be exact (36). Here, the situation is more complex because the cytosol is a viscoelastic medium and a quantitative determination of the force would require knowledge of the complete viscoelastic response function (see Levine and Lubensky (37) for the response function of a model system).

Note that it is not clear whether the force is a repelling force acting between the centrosomes or an attractive force acting from the outside and pulling the centrosomes apart. Here, we merely use the intrapair distance as a measure for the distance of the centrosomes from their midpoint, i.e., the center of their nucleus. This allows us to circumvent the problem of the global drift movement, which we do not know.

Assuming a Gaussian approximation to the probability density  $p_{r_0}(r, \tau)$  of the separation  $r$  after time  $\tau$ , given a separation  $r_0$  at time 0,

$$p_{r_0}(r, \tau) = \frac{1}{\sqrt{2\pi\tau s}} \exp\left(-\frac{(r - r_0 - v_{r_0}\tau)^2}{2s^2\tau}\right), \quad (5)$$

with the radial speed  $v_{r_0}$  and the diffusion constant  $s^2$ , we see that this is the solution of a diffusion equation

$$\frac{\partial}{\partial \tau} p_{r_0} = -v_{r_0} \frac{\partial}{\partial r} p + \frac{1}{2} s^2 \left(\frac{\partial}{\partial r}\right)^2 p. \quad (6)$$

This equation is what one would expect for particles subject to a random force (the second term) plus a deterministic force (the first term). It can indeed be derived from a more fundamental Langevin equation and its corresponding Fokker-Planck equation but, as mentioned above, only for a purely viscous system. Nevertheless, it shows again the qualitative connection between the radial speed  $v_{r_0}$  and the deterministic force acting at distance  $r_0$ .

The assumption of a Gaussian distribution is only justified for small  $\tau$  when the particles did not have time to move far. In our experiments, we are limited to larger values of  $\tau$ , and we observe deviations from the Gaussian behavior (see Fig. 1 G). However, qualitatively, the argument that a force induces a temporal increase of the average separation remains intact.

## RESULTS

### Analysis of centrosomal mobility and fluctuations

To assay microtubule network dynamics *in vivo*, we established a quantitative assay for recording and analyzing centrosome movement at a temporal resolution of one image per second in syncytial *Drosophila* embryos. We imaged centrosomes, which are associated with the (–)-ends and form the microtubule organizing centers. Representing the nodes of the microtubule network, centrosomes dynamics may serve as a proxy for the microtubule network dynamics. The centrosomes were genetically labeled by GFP-tagged components of the centrioles (Sas4-GFP, Sas6-GFP).

We first determined the trajectories of centrosomes by image segmentation and tracking (see Image Analysis and

Tracking, above). For detection, we developed a maximum likelihood approach, taking into account the complete image generation process and additional information such as sparsity constraints, which are known a priori about the system. This approach has the benefit that it is nonheuristic and can naturally deal with background signals, which are spatially and temporally slowly varying, thus avoiding user interaction.

At the end of mitosis, the centrosomes move from the spindle poles to an apical position between the cortex and the newly formed daughter nuclei (Fig. 1 A and Movies S1 and S2). Soon after this movement, duplication leads to a pair of centrosomes (Fig. 1 A–C). In our assays, we define the time of duplication as  $t = 0$ . During interphase, the centrosome pair separates and the centrosomes subsequently move to opposing equatorial positions in the nucleus before the next mitosis (Fig. 1, A and B). The equatorial movement has been analyzed previously by slow time-lapse recording and shown to be dependent on F-actin (5,38). The mechanisms determining the movement during initial pair separation have not been analyzed.

We first extracted a time series of pair distances  $r$  from our movies (Fig. 1, D and E). The minimal pair distance that we can detect is in the range of 0.5  $\mu\text{m}$ . The average pair distance increased first slowly and then rapidly before mitosis and nuclear envelope breakdown, as described previously in Cao et al. (5). The pair distance at the end of each interphase, except interphase 14, corresponds to the equatorial distance. This distance decreases with each interphase, as the nuclei become smaller. In interphase 14, centrosome pairs persist, as mitosis 14 occurs only 1 h later in development. As initial pair separation and equatorial movement are two distinct processes, we focus in the following only on cycle 14, which does not include an equatorial movement.

### Role of F-actin in initial separation of centrosome pairs

We regard motion of the centrosome pairs as a superposition of directed and diffusionlike movement. We applied a statistical analysis of the fluctuations to separate these two components. The approach and its justification is explained in Radial Speed: A Qualitative Measure for Centrosomal Forces. By analyzing the time series of individual pair distances, fluctuations became obvious (Fig. 1 F). We divided the pair distances  $r$  into bins of 0.5- $\mu\text{m}$  width and collected all pair distance changes  $\Delta r$ , which happened within each bin after a time  $\tau$  had passed (Fig. 1 F, inset) and plotted the distribution of  $\Delta r$  for each bin (Fig. 1 G). This was done for a range of  $\tau$ -values. We observed that the averages of these distributions (Fig. 1 G, dotted vertical lines) increased with  $\tau$  as a function of the initial pair distance. For each initial pair distance, we hence estimated the radial speed by applying a linear fit to the average pair distance as a function of  $\tau$  (Fig. 1 G, inset).

The result is shown in Fig. 1 *H*. In a simplified model, in which the centrosomes are considered to be spherical particles moving in a purely viscous medium and subject to both Gaussian random forces and a distance-dependent deterministic force, the average speed is, in fact, up to a constant factor equal to the force (see also Sainis et al. (36)). In our case, the situation is more complicated, as the medium is viscoelastic. In principle, the complete response function of the medium needs to be known to calculate the forces from the radial speeds (see, e.g., Levine and Lubensky (37,39)). (For a theoretical description, see MacKintosh and Schmidt (40), Weihs et al. (41), and Wirtz (42); and for an overview, see Radial Speed: A Qualitative Measure for Centrosomal Forces.) In addition, the medium is inhomogeneous, containing organelles of the same length scale as the centrosomes, which makes a continuum description difficult. Nevertheless, our measurements indicate that up to a distance of 3–4  $\mu\text{m}$ , the pairs separate systematically, whereas centrosomes move independently with no significant radial speed for larger distances. These findings suggest a corresponding range of pair separation forces of  $\sim 2\text{--}3 \mu\text{m}$ . Due to the caveat that the medium is not purely viscous and inhomogeneous, Fig. 1 *H* is a qualitative measure of the force.

Centrosome movement is driven by microtubules and F-actin (5,6,38). Previously, it has been shown that centrosome movement to the nuclear equator before nuclear envelope breakdown in mitosis depends on both microtubules and F-actin (5). We tested the contribution of F-actin to active directional movement (radial speed) by recording centrosome movements in embryos treated with latrunculin. Consistent with previous reports (5), centrosomes separated up to a pair distance of 2–4  $\mu\text{m}$  (Fig. 1, *D* and *E*). Based on this data set, we again calculated radial speed as a function of pair distance (Fig. 1 *H*). In contrast to wild-type embryos, radial speed was close to zero, even at small pair distances of 1 or 2  $\mu\text{m}$ . This indicates that F-actin is involved in separation of centrosome pairs by promoting directional movement.

Our fluctuation analysis suggests that the centrosome pair separation is driven by directed forces, which are active up to a distance of  $\sim 3\text{--}4 \mu\text{m}$ . These directed forces depend on F-actin. At larger distances or in latrunculin-injected embryos, the centrosomes move in a diffusive manner at all distances.

### Fluctuation parameter for fast centrosomal mobility

In the following, we analyzed the movement of single centrosomes. Visual inspection of the centrosome movies indicate that their movement consists of a random motion on a short timescale, superimposed on large-scale drift movements together with their neighbors (Fig. 2 *A* and Movies *S1* and *S2*). The latter was particularly pronounced shortly after mitosis. Two different types of network interactions

may be important for active movement (Fig. 2 *B*). Lateral interactions exist between the centrosome pairs and their associated asters and cortical interactions of the centrosomes with the actin cortex beneath the embryonic plasma membrane.

To separate the fast and slow movements of single centrosomes, we define for each centrosome  $i$  the deviation,  $d_i(t)$ , from directional movement using three time points (see Fig. 2 *C* and Fluctuations). The fluctuation parameter  $D_i(t) = d_i^2(t)/\Delta t$  is then defined, assuming equidistant time stepping  $\Delta t$  (see Eq. 2). The fluctuation parameter  $D_i(t)$  captures the fast fluctuations around a spatially and temporally slowly varying global drift and can be calculated without knowledge of the drift and without considering the trajectories of any of the neighbors. Thus, the average  $D(t) = (1/N_t) \sum_{i=1}^{N_t} D_i(t)$ , where  $N_t$  is the number of centrosomes present (and visible) at time  $t$ , is insensitive to drift, irregular overall arrangement of centrosomes, and loss of centrosomes.

This is in contrast to a more conventional approach using the mean-square displacement (MSD). For a normal diffusive process in the absence of drift, the MSD increases linearly with time. In that case, the slope is a measure of the diffusion constant. To illustrate the different sensitivities toward drift of MSD and  $D(t)$ , we have performed simulations of a single particle subject to diffusion and a circular drift (Fig. 2 *D*). In this setting, the MSD depends unsystematically on time, whereas the fluctuation parameter remains stationary and thus is insensitive to drift.

We calculated the time series of  $D(t)$  from movies of blastoderm embryos in interphase 14. (Fig. 2 *E* and Movie *S2*). Centrosome duplication was set to  $t = 0$  (Fig. 2 *E*), i.e., each centrosome is equipped with its own clock calibrated in such a way that the time of last duplication is set to 0. We found that the fluctuations of centrosomes are more variable before but become quite stable after centrosome duplication. As  $D$  remained comparatively constant in the interphase, we averaged  $D$  over the period between 60 and 260 s to obtain a time-independent parameter.

To test the sensitivity of  $D$  toward experimental conditions, we first compared the two centrosome labels, Sas4 and Sas6. With both types of embryos we obtained consistent results with  $D$  in the range of  $4\text{--}5 \times 10^{-3} \mu\text{m}^2/\text{s}$ . Our measurements are insensitive toward illumination conditions over a broad range (Fig. 2, *F* and *G*, and Table *S1*). This is important as the signal-noise ratio deteriorates over time due to bleaching.

Our measurements reflect an active and energy-dependent behavior of centrosomes. Embryos depleted of ATP by injection of the poison sodium azide showed a threefold reduced  $D$  (Fig. 2 *F*). This value was in a range similar to what we measured in fixed embryos and reflects the measurement error in the positions of the centrosomes and possibly the thermal movement of the label (Fig. 2 *F*). Surprisingly, after these treatments, we still measured nonzero

fluctuations. These fluctuations may be due to measurement error or thermal movement. The small difference between azide-treated and fixed embryos may be due to differences in the viscoelastic properties, which affect thermal movement. These measurements hence provide an upper limit of the measurement error, which can be inferred from Eq. 4 to be  $\sigma \leq \sqrt{(\Delta t/3)D} \approx 0.026 \mu\text{m}$ . For our simulations (see below), we therefore chose a value of  $\sigma = 0.016 \mu\text{m}$  compatible with this upper limit, and which is an order of magnitude below the pixel size. Because the thermal fluctuations and measurement errors account for at most one-third of the normal fluctuations, unknown active processes appear to be responsible for a large part of the fluctuations.

On the one hand, the part of  $D$  that depends on the measurement error diverges with decreasing  $\Delta t$  (see Fluctuations). On the other hand, increasing  $\Delta t$  leads to dependence on the drift, which can no longer be considered constant between frames. We calculated the frame-rate dependence of  $D$  for one particular set of data (one wild-type embryo in interphase 14). We extended our normal imaging protocol toward a faster frame rate of 20 Hz. The value  $D$  is lowest at  $\sim 1$  Hz. As expected, it increases for both lower and higher  $\Delta t$ . It rises to a plateau between 10 and 30 s (Fig. 2 H), reflecting the influence of the drift. For  $\Delta t < 0.5$  s, we observed a sharp increase.

To confirm our interpretation that the increase of  $D$  is due to either drift movement or measurement error, we computationally generated three data sets of a fluctuating particle in a velocity field, obtained as the solution of a stochastic differential equation. The first is the trajectory of the particle in a spatially and temporally constant flow field (i.e., linear drift). The second is the trajectory in a circular flow field,

constant in time (i.e., circular drift). The third one is the same as the second but with additional noise (i.e., circular drift with errors, Fig. 2 I). As expected, the fluctuation parameter  $D$  becomes sensitive to the drift movement at longer frame intervals, whereas at small frame intervals, the measurement error starts to dominate. The smallest influence of drift and measurement error is found between these two regimes and lies in the range of seconds for our chosen sets of parameters. It should be noted, however, that the precise location of the minimum depends on those parameters. The simulation confirms the existence of the experimentally observed minimum and indicates that the regimes dominated by drift and by measurement error are sufficiently separated. With the experimentally determined minimum at a frame interval of  $\sim 1$  s, we performed all subsequent measurements at a rate of 1 Hz.

### Cortical actin caps suppress centrosomal fluctuations

The fluctuations of centrosomes may reflect passive thermal movements of the cytoplasm or active fluctuations of the dynamical cytoskeletal networks. To distinguish these options, we depolymerized F-actin by injection of latrunculin in comparison to injection of water (Fig. 3, A and B, Movie S3, and Table S2). Surprisingly, depolymerization of F-actin resulted in an approximately twofold increase in  $D$  from  $5.6 \times 10^{-3}$  to  $11 \times 10^{-3} \mu\text{m}^2/\text{s}$  and thus uncovered a suppressive function of F-actin on centrosomal mobility (Fig. 3 C). This increased mobility after F-actin depolymerization is due to active, microtubule-based movement, and not unrestricted thermal/passive movement. We found that

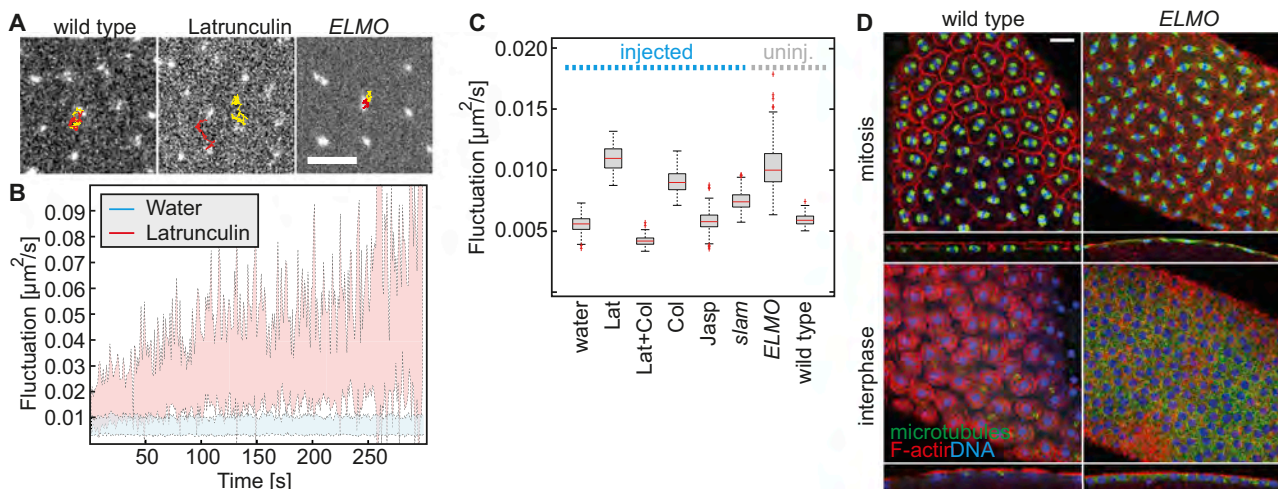


FIGURE 3 Cortical actin caps suppress fluctuations. (A) Images from time-lapse recordings of wild-type, latrunculin-injected, and *ELMO* embryos expressing Sas6-GFP. Centrosome trajectories (120 s) are marked (red and yellow). Scale bar =  $5 \mu\text{m}$ . (B) Time courses of fluctuation (range of standard deviation) in embryos injected with water or latrunculin in mitosis interphase 13. (C) Time-averaged fluctuation in embryos with indicated treatment (injected) or genotype (not injected). Latrunculin (Lat) + Colcemid (Col) coinjection; injected with Jasplakinolide (Jasp); and depleted by *slam* RNAi (*slam*). Statistical significance of all pairs is listed in Table S3. (D) Images of wild-type and *ELMO* embryos stained for F-actin (red), microtubules (green), and DNA (blue). Small images show sagittal section of the same embryo. Scale bar =  $10 \mu\text{m}$ .

coinjection of latrunculin and colcemid lead to a loss of the increased fluctuation to  $D = 4.2 \times 10^{-3} \mu\text{m}^2/\text{s}$ , in the range of the value measured in water-injected embryos (Fig. 3 C and see Movie S4). Depolymerization of microtubules by injection of colcemid also lead to increased fluctuations with  $D = 9.1 \times 10^{-3} \mu\text{m}^2/\text{s}$  (Fig. 3 C). Thus, microtubules also stabilize centrosome movement and may have a dual function, as they are also required for stronger fluctuations in the absence of F-actin. Conversely to depolymerization, stabilization of F-actin by Jasplakinolide (Jasp) did not affect fluctuations, indicating that the assembly-disassembly cycle of actin filaments is not required for suppression of fluctuations by F-actin (Fig. 3 C).

During interphase, F-actin accumulates in actin caps above centrosomes. To assess whether the caplike distribution of F-actin is important for centrosome mobility, we employed *ced-12/ELMO* mutant embryos that lack actin caps and display uniform cortical actin (Fig. 3 D). The *ced-12/ELMO* embryos pass through syncytial cell cycles with a timing comparable to wild-type embryos (data not shown). However, metaphase furrows did not form (Fig. 3 D), chromosome segregation defects were frequently observed, and cellularization failed (data not shown). We introduced the centrosome marker Sas6-GFP into these embryos and recorded centrosome movement. We measured an average of  $D = 10.3 \times 10^{-3} \mu\text{m}^2/\text{s}$ , which lies in the range of  $D$  that we measured in latrunculin-injected embryos (Fig. 3 C and see Movie S5). These data suggest that the organization of F-actin into caps is important for the suppression of centrosome fluctuations. Unstructured cortical F-actin as present in *ced-12/ELMO* mutants does not suffice for stabilization of centrosomes.

During interphase 14, development switches from syncytial to cellular development. The plasma membrane invaginates between adjacent nuclei to enclose nuclei into individual cells. Furrow invagination is associated with reor-

ganization of F-actin. The cortical actin caps dissolve, while the furrow canal, the tip of the invagination membrane, acquires an actin coat. We tested whether centrosomal fluctuations are affected by this reorganization in cellular and cytoskeletal structure by analyzing *slam* mutant embryos. *Slam* is required for invagination of furrows. We depleted *slam* by injection of *slam* dsRNA into embryos expressing the centrosomal marker Sas6-GFP. Induction of the mutant phenotype was verified by the absence of furrow invagination. Quantification of centrosome fluctuations in these embryos revealed a slight increase of fluctuations with  $D = 7.5 \times 10^{-3} \mu\text{m}^2/\text{s}$  (Fig. 3 C). These data suggest that the invaginating furrows may only weakly suppress fluctuations.

### Role of molecular motors Myosin-II and Kinesin-1

Active fluctuations of the centrosomes may be promoted by molecular motors. Potential candidates are myosin motor proteins for the actin cytoskeleton. To assess the role of non-muscle Myosin-II, we interfered with its function by inhibiting Rho kinase, which is a well-characterized activator of Myosin-II by injection of the chemical inhibitor Y-27632 (5). Its functionality was verified by the loss of localized fluorescence of Myo-II-GFP (data not shown). We recorded movies of Y-27632-injected embryos expressing Sas6-GFP. The calculated centrosomal fluctuations were slightly increased to  $D = 8.1 \times 10^{-3} \mu\text{m}^2/\text{s}$ , which corresponds to an ~50% increase as compared to water-injected embryos (Fig. 4 C). Thus, these data suggest that Myosin-II, as much as it is affected by the inhibition of Rho kinase, does not promote centrosomal fluctuations but rather contributes to suppression of fluctuations by F-actin.

Concerning molecular motors of the microtubules, a prime candidate is Kinesin-1. Kinesin-1 is not required for mitosis, and mutant embryos could be obtained (14).

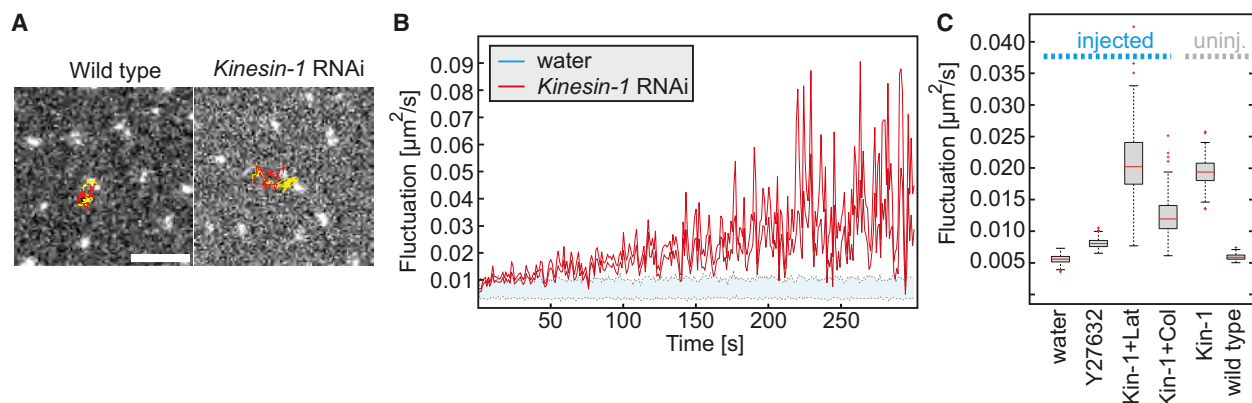


FIGURE 4 Kinesin-1 suppresses centrosome fluctuations. (A) Images from time-lapse recordings of wild-type and *Kinesin-1* mutant embryos expressing centrosomal GFP markers. Centrosome trajectories (120 s) are marked (red and yellow). Scale bar = 5  $\mu\text{m}$ . (B) Time courses of fluctuation (range of standard deviation) in wild-type and *Kinesin-1* mutant embryos. (C) Time-averaged fluctuation in embryos with indicated treatment (injected) or genotype (not injected). Injection of latrunculin (Lat), colcemid (Col), or an inhibitor of Rho kinase (Y27632). Kinesin-1 depleted by *Kinesin-1* RNAi. Statistical significance of all pairs is listed in Table S3.

*Kinesin-1* mutant embryos developed normally until interphase 14 but did not cellularize (Fig. S1 and Movies S6, S7, S8, and S9). Expression of *Kinesin-1* dsRNA in the germline leads to a similar phenotype. Furthermore, *ens* mutant embryos showed a similar phenotype (Fig. S1). *Ens* functions together with *Kinesin-1* and is involved in loading of *Kinesin-1* onto microtubules (14). In the following, we employed *Kinesin-1* RNA<sub>i</sub> for the sake of experimental simplicity. We first stained wild-type and *Kinesin-1* mutant embryos for F-actin and microtubules (data in Fig. S2, A and B). We did not observe any difference in microtubule asters during syncytial cycles and nuclear baskets in interphase 14. F-actin distribution, i.e., actin caps in interphase and metaphase furrows during mitosis, was also similar in wild-type and *Kinesin-1* mutants. We recorded centrosomal fluctuations in embryos expressing *Kinesin-1* dsRNA and Sas4-GFP (Fig. 4 A). Surprisingly, *Kinesin-1* was required for suppression of centrosome fluctuation rather than promotion, as one might expect for a motor (Fig. 4 B). The fluctuation parameter  $D$  increased by more than threefold as compared to wild-type embryos to  $D = 19.4 \times 10^{-3} \mu\text{m}^2/\text{s}$  (Fig. 4 C and Table S2). These data suggest that the microtubule motor *Kinesin-1* is involved in suppression of centrosome mobility. The increased fluctuation in embryos depleted for *Kinesin-1* was not further increased by injection of latrunculin (Fig. 4 C). As actin depolymerization in *Kinesin-1* mutants did not increase the fluctuations, cortical actin and *Kinesin-1* may act in the same pathway. Conceivably, *Kinesin-1* may

establish the linkage between the microtubule network and the cortical actin caps.

In contrast, the increased fluctuations in *Kinesin-1*-depleted embryos depended partly on microtubules. Depolymerization of microtubules by injection of colcemid reduced fluctuations to  $D = 12.7 \times 10^{-3} \mu\text{m}^2/\text{s}$ . This indicates that the fluctuation movements uncovered after depletion of *Kinesin-1* are mediated by microtubules and conceivably by motors other than *Kinesin-1*. This observation disfavors an alternative model for *Kinesin-1* function, namely in lateral interactions: in such a model, *Kinesin-1* cross-links overlapping microtubule asters and stabilizes the microtubule network. Correspondingly, loss of *Kinesin-1* would lead to higher mobility of the loosened centrosomes. An additional depolymerization of microtubules on top of *Kinesin-1* depletion would not change the mobility.

A prediction of a function of *Kinesin-1* in cortical interactions of the microtubule network is a localization of *Kinesin-1* at the cortex. Hence, we analyzed the distribution of *Kinesin-1* protein. We imaged *Kinesin-1* in transgenic flies expressing *Kinesin-1*-GFP (14). Movies of such embryos showed that *Kinesin-1*-GFP accumulated at cortical actin caps in interphase and spindles in mitosis (Fig. 5, A and B). Such a cortical localization of *Kinesin-1* is consistent with a function of *Kinesin-1* in linking microtubule asters to the cortex. Astral microtubules are oriented with their (+)-ends toward the cortical actin caps, where the (+)-end directed motor *Kinesin-1* accumulates and may serve as a

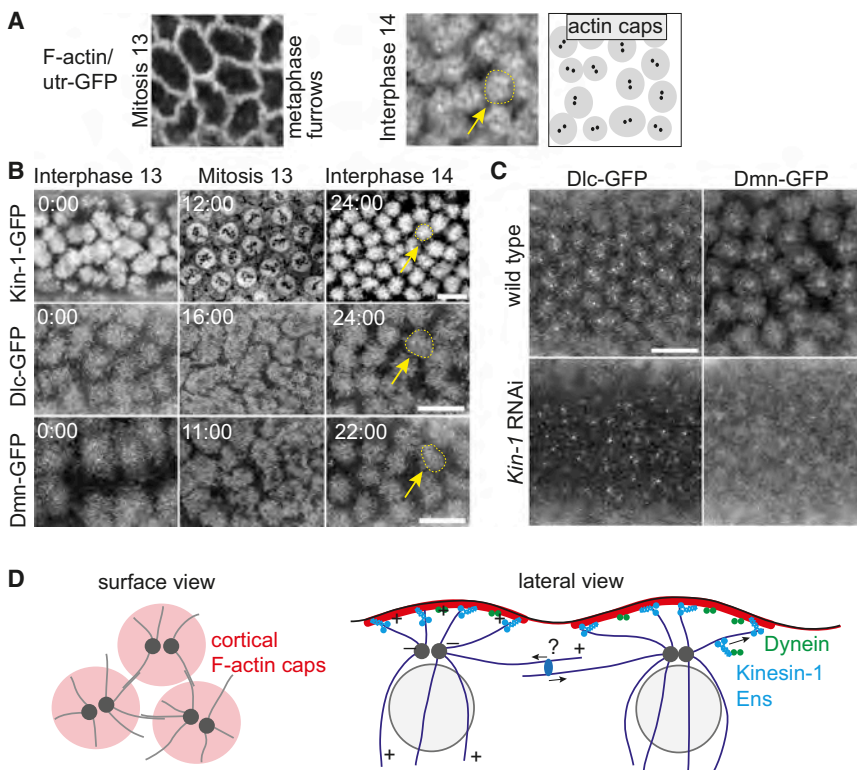


**FIGURE 5** *Kinesin-1* is required for cortical Dynein. Images from time-lapse recordings of embryos expressing (A) F-actin marker utr-GFP (utrophin); (B) *Kinesin-1*-GFP; and (B and C) Dlc-GFP (Dynein light chain) and Dmn-GFP (Dynamitin) between interphases 13 and 14. (A) Scheme indicates structure of actin caps (arrow, dashed circle) with centrosome pairs (black dots) in interphase. (C) Images of wild-type and *Kinesin-1* mutant embryos in interphase 14. (D) Model for the interaction of centrosomes with the cortex and suppression of centrosome fluctuations by cortical F-actin and *Kinesin-1*. Scale bars = 10  $\mu\text{m}$ .

linker between the (+)-ends of the microtubules and F-actin (Fig. 5 D).

The function and subcellular dynamics of Kinesin-1 has not yet been investigated in early *Drosophila* embryos, to our knowledge. Previously, a function of Kinesin-1 in germ plasm formation during oogenesis and subsequent anterior-posterior pattern formation was described in Brendza et al. (10) and Januschke et al. (11). In the developing oocyte, Kinesin-1 transports the (–)-end directed motor Dynein to the posterior cortex, where Kinesin-1 and Dynein colocalize and are assumed to anchor germ plasm and posterior determinants. For the early embryo, it has been reported that Dynein accumulates at the actin caps (43), although its functions have remained unclear. It is assumed that Dynein contributes to formation and function of the mitotic spindle. The mechanism for its localization at the cortical actin caps in interphase has remained unknown, however. We tested whether the presence of Dynein at the cortex depends on Kinesin-1 in the blastoderm embryo. We confirmed the cortical localization of Dynein with movies of transgenic embryos expressing two components of the Dynein complex, either Dlc-GFP (Dynein light chain) or Dmn-GFP (Dynamitin) (15). Cortical localization of the Dynein complex depended on *Kinesin-1* (Fig. 5 C). Embryos, in which *Kinesin-1* was depleted by RNA<sub>i</sub>, lost the clear cortical caplike localization of both Dlc-GFP and Dynamitin-GFP, whereas the centrosomal signal remained clear (Fig. 5 C). These data suggest that cortical localization of Dynein depends on Kinesin-1, whereas other aspects of Dynein localization, such as centrosomal localization, are independent of Kinesin-1.

## DISCUSSION

Our data are consistent with a model that Kinesin-1 mediates cortical anchoring of microtubule asters (Fig. 4 D). This extends a previous model that Dynein links mitotic spindles to the cortex in syncytial embryos and contribute to lengthening of the spindle in anaphase (43). The previously proposed model is focused on mitosis and does not provide an explanation for a potential function and for the localization of the (–)-end directed motor Dynein in the region of the (+)-ends of microtubules asters in interphase. We propose that interactions between the microtubule network and the actin cortex are comparable in interphase and during mitosis, both involving cortical microtubule motors as a link between microtubules and cortical actin. Kinesin-1 may directly interact with components of the actin cap and anchor the microtubule (+)-ends to the cortex. In this model the dependence of cortical Dynein localization on Kinesin-1 would not be relevant for microtubule anchoring. Alternatively, Kinesin-1 may act indirectly, in that it transports Dynein to the (+)-ends with the help of Ensconsin. After reaching the cortex, Dynein then serves as an anchor for microtubules. As both models are

not mutually exclusive, Kinesin may first transport Dynein to the cortex and then together with Dynein provide a cortical link.

Such a function of Kinesin-1 would not have been discovered by analysis of static images or slow movies. In contrast to more severe interference, such as depolymerization of F-actin, which leads to visible morphological defects, the cytoskeletal organization, as seen in fixed embryos, is not obviously disturbed. The differences in cytoskeletal mobility between wild-type and mutant embryos, however, are revealed by the dynamics of centrosomes.

The dynamics of the cytoskeleton in the complex embryo is determined by multiple parameters acting on many length and timescales. We introduced a fluctuation parameter, which allowed us to separate large-scale and slow (range of minutes) drift movement from fast stochastic motion in a timescale relevant for cytoskeletal dynamics. If the density was high enough, the drift could be estimated by averaging over the movement of several neighbors. In mutant or injected embryos with irregular morphology, neighborhood relations are difficult to establish, however.

We also addressed the question of whether the structure of cortical actin is important for stabilization of centrosomal mobility by comparing wild-type with caplike organization and mutant embryos with uniform F-actin distribution (*ced-12/ELMO* mutants). We provide evidence that the caplike structuring of cortical actin clearly contributes to stabilization of centrosomal mobility, as fluctuations were similar in latrunculin-injected and *ced-12/ELMO* embryos. Interesting in this respect is the fact that the F-actin caps are induced by the underlying centrosomes (4) and that caps feed-back to influence centrosome mobility, effectively constituting a mutual functional relationship.

So far, we have identified only components that stabilize centrosome fluctuations. Indirect inhibition of Myosin-II and depletion of Kinesin-1 both lead to increased fluctuations. For a motor driving centrosome mobility, we would expect a reduced fluctuation parameter  $D$ , if this motor is inhibited or genetically depleted. Based on our data, we expect that active components exist and that they act on both F-actin and microtubules. Depolymerization of both F-actin and microtubules lead to a reduced fluctuation parameter  $D$ , whereas depolymerization of either F-actin or microtubules lead to an increased  $D$ . This indicates that a microtubule-dependent motor drives the higher fluctuation in the case of F-actin depolymerization, and an F-actin-dependent motor, in the case of microtubule depolymerization. Furthermore, depolymerization of microtubules in *Kinesin-1*-depleted embryos lead to reduced fluctuations. This indicates that the increased centrosomal mobility in such embryos depends on intact microtubules. The high fluctuations may be due to a microtubule motor.

A promising candidate for the microtubule network is Kinesin-5, which is a four-headed molecular motor

involved in antiparallel sliding of microtubules and in spindle elongation during mitosis (44–46). During mitosis, Kinesin-5 is involved in antiparallel sliding of microtubules. This activity is assumed to contribute to elongation of the spindle in anaphase. Kinesin-5 may have a similar function during interphase in syncytial embryos. Using a GFP-tagged Kinesin-5 we have observed dynamical localization of Kinesin-5 on the microtubule asters (unpublished data). Kinesin-5 may locate at positions, where microtubules from adjacent microtubule asters arrange in an antiparallel manner and may contribute to repulsion of adjacent asters.

In this study, we employed an approach to analyze the dynamics of centrosomes in that the individual paths including fluctuations were treated as a source of information instead of being simply averaged. The fluctuations are caused by thermal forces and importantly, active nonequilibrium forces of the actin and microtubule cytoskeleton. The contribution by active forces was uncovered by depolymerization of the cytoskeleton. Ideally, we would like to record centrosome dynamics in a frequency space of up to 100 Hz, providing a more comprehensive description of the material properties of the embryo. Together with the yet-to-be-determined viscoelastic properties of the embryos, this would allow quantification of the active force contribution by the cytoskeleton. However, we are limited to frame rates in the second range with GFP-based probes. Using innovative fluorescent labels such as single-walled carbon nanotubes targeted to centrosomes may provide a means to overcome the limits of GFP labels (8).

## SUPPORTING MATERIAL

Two figures, three tables, and nine movies are available at [http://www.biophysj.org/biophysj/supplemental/S0006-3495\(15\)00779-1](http://www.biophysj.org/biophysj/supplemental/S0006-3495(15)00779-1).

## AUTHOR CONTRIBUTIONS

J.G. designed the experimental approach; A.Z. and T.A. conceived the method for quantitative data analysis; M.G. and F.W. performed the experiments; L.K. performed the data analysis; and Z.L. conducted the experiments concerning *ELMO*.

## ACKNOWLEDGMENTS

We thank M. Baylies, M. Bettencourt-Dias, T. Hays, T. Lecuit, P. Rorth, J. Raff, F. Schnorrer, H. Sung, and S. Tsukita, and the Developmental Hybridoma Band at the University of Iowa, the Bloomington *Drosophila* Stock Center, the Genomic Resource Center at Indiana University, and the Transgenic RNAi Project at Harvard Medical School (funded by grant No. RO1-GM084947 from the National Institutes of Health/National Institute of General Medical Sciences) for discussions, materials, or fly stocks. We thank T. Kanesaki for initial work.

This work was supported in part by the German Research Council (under Sonderforschungsbereich (SFB) grant No. 937/TP A10).

## REFERENCES

1. Foe, V. E., G. M. Odell, and B. A. Edgar. 1993. Mitosis and morphogenesis in the *Drosophila* embryo: point and counterpoint. In *The Development of Drosophila melanogaster*. M. Bate and A. Martinez Arias, editors. Cold Spring Harbor Laboratory Press, Cold Spring Harbor, NY.
2. Schejter, E. D., and E. Wieschaus. 1993. Functional elements of the cytoskeleton in the early *Drosophila* embryo. *Annu. Rev. Cell Biol.* 9:67–99.
3. Kanesaki, T., C. M. Edwards, ..., J. Grosshans. 2011. Dynamic ordering of nuclei in syncytial embryos: a quantitative analysis of the role of cytoskeletal networks. *Integr. Biol. (Camb)*. 3:1112–1119.
4. Raff, J. W., and D. M. Glover. 1989. Centrosomes, and not nuclei, initiate pole cell formation in *Drosophila* embryos. *Cell*. 57:611–619.
5. Cao, J., J. Crest, ..., W. Sullivan. 2010. Cortical actin dynamics facilitate early-stage centrosome separation. *Curr. Biol.* 20:770–776.
6. Robinson, J. T., E. J. Wojcik, ..., T. S. Hays. 1999. Cytoplasmic dynein is required for the nuclear attachment and migration of centrosomes during mitosis in *Drosophila*. *J. Cell Biol.* 146:597–608.
7. Sommi, P., D. Cheerambathur, ..., A. Mogilner. 2011. Actomyosin-dependent cortical dynamics contributes to the prophase force-balance in the early *Drosophila* embryo. *PLoS One*. 6:e18366.
8. Fakhri, N., A. D. Wessel, ..., C. F. Schmidt. 2014. High-resolution mapping of intracellular fluctuations using carbon nanotubes. *Science*. 344:1031–1035.
9. Yang, J. T., W. M. Saxton, and L. S. Goldstein. 1988. Isolation and characterization of the gene encoding the heavy chain of *Drosophila* kinesin. *Proc. Natl. Acad. Sci. USA*. 85:1864–1868.
10. Brendza, R. P., L. R. Serbus, ..., J. B. Duffy. 2002. Posterior localization of dynein and dorsal-ventral axis formation depends on kinesin in *Drosophila* oocytes. *Curr. Biol.* 12:1541–1545.
11. Januschke, J., L. Gervais, ..., A. Guichet. 2002. Polar transport in the *Drosophila* oocyte requires Dynein and Kinesin-I cooperation. *Curr. Biol.* 12:1971–1981.
12. Metzger, T., V. Gache, ..., M. K. Baylies. 2012. MAP and kinesin-dependent nuclear positioning is required for skeletal muscle function. *Nature*. 484:120–124.
13. Pilling, A. D., D. Horiuchi, ..., W. M. Saxton. 2006. Kinesin-1 and Dynein are the primary motors for fast transport of mitochondria in *Drosophila* motor axons. *Mol. Biol. Cell*. 17:2057–2068.
14. Sung, H. H., I. A. Telley, ..., P. Rørth. 2008. *Drosophila* Ensconsin promotes productive recruitment of Kinesin-1 to microtubules. *Dev. Cell*. 15:866–876.
15. Wojcik, E., R. Basto, ..., T. Hays. 2001. Kinetochore dynein: its dynamics and role in the transport of the Rough deal checkpoint protein. *Nat. Cell Biol.* 3:1001–1007.
16. Peel, N., N. R. Stevens, ..., J. W. Raff. 2007. Overexpressing centriole-replication proteins in vivo induces centriole overduplication and de novo formation. *Curr. Biol.* 17:834–843.
17. Luschnig, S., B. Moussian, ..., C. Nüsslein-Volhard. 2004. An F1 genetic screen for maternal-effect mutations affecting embryonic pattern formation in *Drosophila melanogaster*. *Genetics*. 167:325–342.
18. Mazzalupo, S., and L. Cooley. 2006. Illuminating the role of caspases during *Drosophila* oogenesis. *Cell Death Differ.* 13:1950–1959.
19. Rauzi, M., P.-F. Lenne, and T. Lecuit. 2010. Planar polarized actomyosin contractile flows control epithelial junction remodelling. *Nature*. 468:1110–1114.
20. Oda, H., and S. Tsukita. 2001. Real-time imaging of cell-cell adherens junctions reveals that *Drosophila* mesoderm invagination begins with two phases of apical constriction of cells. *J. Cell Sci.* 114:493–501.
21. Schnorrer, F., K. Bohmann, and C. Nüsslein-Volhard. 2000. The molecular motor dynein is involved in targeting swallow and bicoid RNA to the anterior pole of *Drosophila* oocytes. *Nat. Cell Biol.* 2:185–190.

22. Wenzl, C., S. Yan, ..., J. Grosshans. 2010. Localization of RhoGEF2 during *Drosophila* cellularization is developmentally controlled by Slam. *Mech. Dev.* 127:371–384.
23. Hafi, N., M. Grunwald, ..., P. J. Walla. 2014. Fluorescence nanoscopy by polarization modulation and polarization angle narrowing. *Nat. Methods*. 11. <http://dx.doi.org/10.1038/nmeth.2919>.
24. Boufounos, P., M. F. Duarte, and R. G. Baraniuk. 2007. Sparse signal reconstruction from noisy compressive measurements using cross validation. In Proceedings of the IEEE Workshop on Statistical Signal Processing (SSP). Institute of Electrical and Electronics Engineers, Piscataway, NJ, pp. 299–303.
25. Frick, K., P. Marnitz, and A. Munk. 2012. Statistical multiresolution estimation for variational imaging: with an application in Poisson biophotonics. *J. Math. Imaging Vis.* 46:370–387.
26. Babcock, H. P., J. R. Moffitt, ..., X. Zhuang. 2013. Fast compressed sensing analysis for super-resolution imaging using L1-homotopy. *Opt. Express*. 21:28583–28596.
27. Mukamel, E. A., H. Babcock, and X. Zhuang. 2012. Statistical deconvolution for superresolution fluorescence microscopy. *Biophys. J.* 102: 2391–2400.
28. Zhu, L., W. Zhang, ..., B. Huang. 2012. Faster STORM using compressed sensing. *Nat. Methods*. 9:721–723.
29. Fortin, M., and R. Glowinski. 1983. Chapter III. Decomposition-coordination methods using an augmented Lagrangian. In *Augmented Lagrangian Methods: Applications to the Numerical Solution of Boundary-Value Problems*. Elsevier, New York, pp. 97–146.
30. Gal, N., D. Lechtman-Goldstein, and D. Weihs. 2013. Particle tracking in living cells: a review of the mean square displacement method and beyond. *Rheol. Acta*. 52:425–443.
31. Munk, A., N. Bissantz, ..., G. Freitag. 2005. On difference-based variance estimation in nonparametric regression when the covariate is high dimensional. *J. R. Stat. Soc. Series B Stat. Methodol.* 67:19–41.
32. Lau, A. W. C., B. D. Hoffman, ..., T. C. Lubensky. 2003. Microrheology, stress fluctuations, and active behavior of living cells. *Phys. Rev. Lett.* 91:198101.
33. Wessel, A. D., M. Gumalla, ..., C. F. Schmidt. 2015. The mechanical properties of early *Drosophila* embryos measured by high-speed video microrheology. *Biophys. J.* 108:1899–1907.
34. Savin, T., and P. S. Doyle. 2005. Role of a finite exposure time on measuring an elastic modulus using microrheology. *Phys. Rev. E Stat. Nonlin. Soft Matter Phys.* 71:041106.
35. Savin, T., and P. S. Doyle. 2005. Static and dynamic errors in particle tracking microrheology. *Biophys. J.* 88:623–638.
36. Sainis, S. K., V. Germain, and E. R. Dufresne. 2007. Statistics of particle trajectories at short time intervals reveal fN-scale colloidal forces. *Phys. Rev. Lett.* 99:018303.
37. Levine, A. J., and T. C. Lubensky. 2001. Response function of a sphere in a viscoelastic two-fluid medium. *Phys. Rev. E Stat. Nonlin. Soft Matter Phys.* 63:041510.
38. Lim, H. H., T. Zhang, and U. Surana. 2009. Regulation of centrosome separation in yeast and vertebrates: common threads. *Trends Cell Biol.* 19:325–333.
39. Levine, A. J., and T. C. Lubensky. 2000. One- and two-particle microrheology. *Phys. Rev. Lett.* 85:1774–1777.
40. MacKintosh, F. C., and C. F. Schmidt. 1999. Microrheology. *Curr. Op. Coll. Inter. Sci.* 4:300–307.
41. Weihs, D., T. G. Mason, and M. A. Teitell. 2006. Bio-microrheology: a frontier in microrheology. *Biophys. J.* 91:4296–4305.
42. Wirtz, D. 2009. Particle-tracking microrheology of living cells: principles and applications. *Annu. Rev. Biophys.* 38:301–326.
43. Cytrynbaum, E. N., P. Sommi, ..., A. Mogilner. 2005. Early spindle assembly in *Drosophila* embryos: role of a force balance involving cytoskeletal dynamics and nuclear mechanics. *Mol. Biol. Cell.* 16: 4967–4981.
44. Brust-Mascher, I., P. Sommi, ..., J. M. Scholey. 2009. Kinesin-5-dependent poleward flux and spindle length control in *Drosophila* embryo mitosis. *Mol. Biol. Cell.* 20:1749–1762.
45. Heck, M. M., A. Pereira, ..., L. S. Goldstein. 1993. The kinesin-like protein KLP61F is essential for mitosis in *Drosophila*. *J. Cell Biol.* 123:665–679.
46. Sharp, D. J., K. R. Yu, ..., J. M. Scholey. 1999. Antagonistic microtubule-sliding motors position mitotic centrosomes in *Drosophila* early embryos. *Nat. Cell Biol.* 1:51–54.

# Fluctuation analysis of centrosomes reveals a cortical function of Kinesin-1

Franziska Winkler<sup>+</sup>, Maheshwar Gummalla<sup>+</sup>, Lutz Künneke<sup>+</sup>, Zhiyi Lv, Annette Zippelius, Timo Aspelmeier\*, Jörg Grosshans \*

\*Corresponding authors, <sup>+</sup>Equal contribution

## 1 Supplemental material

- Movie 1 Centrosomes marked by Sas-6-GFP in wild type embryo in interphase 13. Maximal intensity projection of multiple axial sections.
- Movie 2 Centrosomes marked by Sas-6-GFP in wild type embryo in interphase 14. Maximal intensity projection of multiple axial sections.
- Movie 3 Centrosomes marked by Sas-6-GFP in embryo in interphase 14 injected with latrunculin during mitosis 13. Maximal intensity projection of multiple axial sections.
- Movie 4 Centrosomes marked by Sas-6-GFP in embryo in interphase 14 injected with latrunculin and colcemid during mitosis 13. Maximal intensity projection of multiple axial sections.
- Movie 5 Centrosomes marked by Sas-6-GFP in embryo from *ELMO*<sup>2L367</sup> germ line clones in interphase 13. Maximal intensity projection of multiple axial sections.
- Movie 6 Development of wild type embryo recorded with wide field optics with differential interference contrast from mitosis 12 to early gastrulation (stage 6/7).
- Movie 7 Development of embryo from *Khc*<sup>27</sup> germ line clone recorded with wide field optics with differential interference contrast from interphase 13 to interphase 14 (cellularization).
- Movie 8 Development of *Kinesin-1* RNAi embryo recorded with wide field optics with differential interference contrast from interphase 13 to early gastrulation.
- Movie 9 Development of embryo from *ens*<sup>sw0</sup> germ line clone recorded with wide field optics with differential interference contrast from mitosis 12 to early gastrulation.

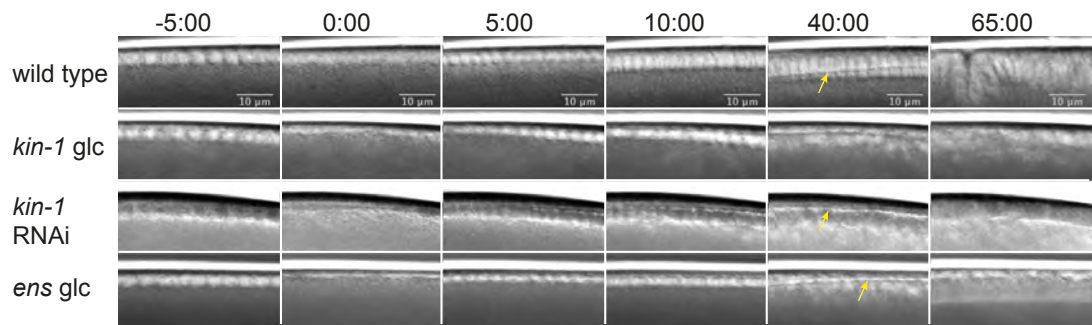


Figure S1: **Cellularization of *Kinesin-1* mutant embryos.** Images from time lapse recordings of wild type, *Khc<sup>27</sup>* (*Kinesin-1*) germline clone (glc), *Kinesin-1* RNAi and *ens* germline clone embryos with wide field optics. Arrows in yellow point to the cellularization front. Time in min:sec. Scale bars 10  $\mu\text{m}$ .

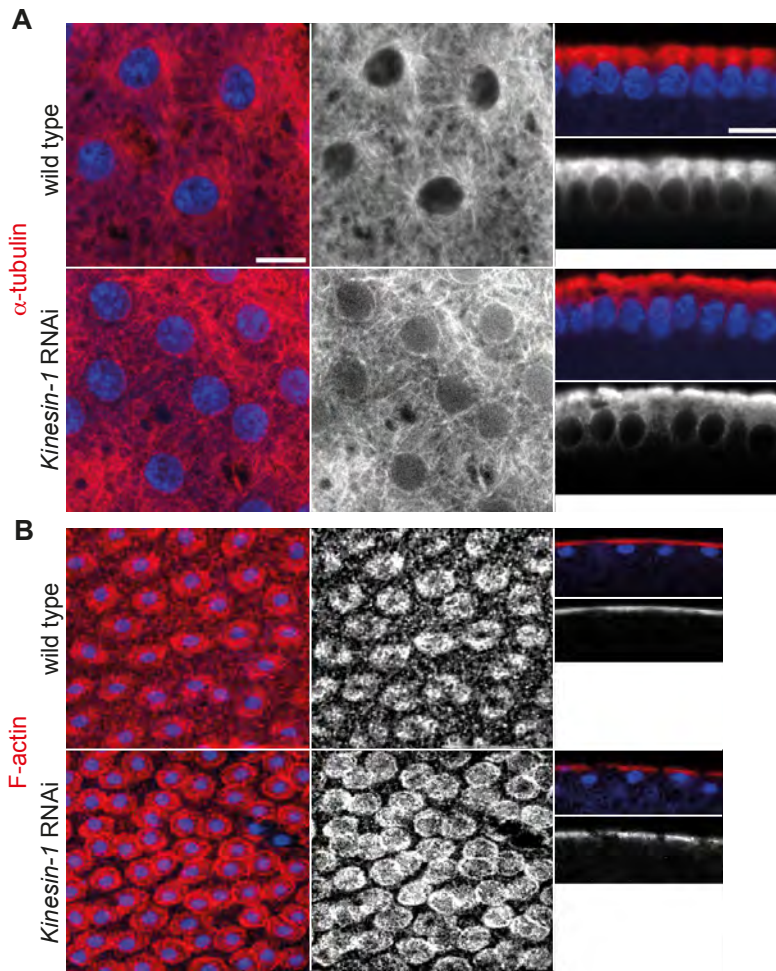


Figure S2: **Microtubules and F-actin in *Kinesin-1* mutant embryos.** Fixed wild type and *Kinesin-1* RNAi embryos were stained for (A) microtubules (red, white) or (B) F-actin (red, white) and DNA (blue). Surface and sagittal sections. Scale bars 10  $\mu\text{m}$ .

Table S1:  
**Quantification of signal noise ratio with  
normal and low illumination**

Time (s)	Illumination	$B$	$\Delta B$	$S$	$S/N$ $= \frac{S-B}{\Delta B}$
0	normal	576.64	18.257	912	18.367
299	normal	559.18	19.223	740	9.406
0	low	555.72	16.963	684	7.563
299	low	550.68	17.625	636	4.841

Signal-to-Noise ratio at the beginning (0 s) and the end (299 s) of a typical movie with normal illumination and a movie with low illumination (1/3 of normal laser intensity). The average  $B$  and the standard deviation  $\Delta B$  of the background signal was determined from a  $30 \times 30$  image region free of centrosomes. The signal  $S$  was determined as the average of the maximum intensity of 4 centrosomes surrounding the background region. Quantities  $B$ ,  $\Delta B$  and  $S$  are given in image grayscale values.

Table S2: **Number of embryos, number of centrosomes and mean of  
fluctuation parameter  $D$**

	Injec- tion	Inter- phase	$N$ embryos	$N$ centro- somes	mean of $D$ $\times 10^{-3}$	STD $\times 10^{-3}$
Wild type	-	11	12	1003	5.45	3.02
Wild type	-	12	16	2250	4.94	0.67
Wild type	-	13	7	1335	8.20	0.88
Wild type	-	14	6	3366	5.93	0.48
Water	+	14	5	1757	5.61	0.68
Latrunculin	+	14	10	3778	11.0	1.06
Latr. + colcemid	+	14	2	657	4.19	0.39
Colcemid	+	14	5	3361	9.05	0.90
Jasplakinolide	+	14	4	922	5.84	0.80
<i>ELMO</i>	-	14	3	711	10.3	1.98
Y-27632	+	14	3	1276	8.11	0.81
<i>slam</i> RNAi	+	14	7	2571	7.51	0.80
<i>Kin-1</i> RNAi	-	14	6	1847	19.4	2.04
<i>Kin-1</i> RNAi + col.	+	14	3	580	12.7	3.14
<i>Kin-1</i> RNAi + lat.	+	14	3	358	20.9	5.25
Sas4	-	14	1	33	4.82	1.25
Fixed	+	14	2	364	1.75	0.40
Azide	+	14	2	228	1.21	0.30

Table S3: Statistical significance of pairwise comparisons (p values)

	WT	Water	Lat	Lat+col	Col	Jasp	<i>ELMO</i>	Y-27632	Slam	Kin-1	Kin Lat	Kin Col
Wild type	1	0.055	7E-158	3E-68	3E-115	0.23	7E-79	2E-83	7E-57	3E-181	8E-95	1E-74
Water		1	2E-180	1E-74	1E-142	4E-03	3E-85	5E-111	5E-81	2E-185	2E-96	3E-78
Lat			1	1E-185	1E-55	1E-171	7E-01	4E-99	2E-122	2E-147	1E-64	3E-08
Lat+col				1	5E-174	3E-66	6E-104	4E-164	9E-148	2E-181	1E-102	4E-91
Col					1	5E-123	4E-11	3E-22	3E-50	2E-165	2E-77	1E-34
Jasp						1	2E-82	6E-87	4E-58	1E-193	6E-96	1E-76
<i>ELMO</i>							1	2E-32	3E-46	2E-154	2E-71	2E-13
Y-27632								1	8E-09	4E-171	5E-83	5E-48
Slam									1	6E-177	2E-87	5E-56
Kin-1										1	3E-4	2E-76
Kin Lat											1	3E-50
Kin Col												1

WT wild type, Lat latrunculin-injected, Col colcemid-injected, Lat+col latrunculin + colcemid co-injected, Jasp jasplakinolide-injected, *ELMO* embryos from *ELMO* germ line clones, Y-27632-injected, Slam *slam* RNAi, Kin-1 *Kinesin-1* RNAi